## Appendix A. Supplementary data

# Ca substitution improves catalytic activity of perovskite $LaCoO_3$ toward toluene: Comprehension in electronic structure alteration

Hanlin Chen [a, c, d], Gaoling Wei [b], Zijuan You [a], Xiaoliang Liang [c, d] *, Peng Liu [e], Yiping Yang [c, d], Fuding Tan [c, d], Suhua Wang [a], Jieqi Xing [c, d], Steven L. Suib [f]

[a] School of Environmental Science and Technology, Guangdong University of Petrochemical Technology, Maoming 525000, P.R. China;

[b] Guangdong Key Laboratory of Integrated Agro-environmental Pollution Control and Management, Guangdong Institute of Eco-environmental Science & Technology, Guangzhou 510650, P.R. China;

[c] CAS Key Laboratory of Mineralogy and Metallogeny/Guangdong Provincial Key Laboratory of Mineral Physics and Materials, Guangzhou Institute of Geochemistry, Chinese Academy of Sciences, Guangzhou 510640, P.R. China;

[d] University of Chinese Academy of Sciences, Beijing 100049, P.R. China;

[e] Guangdong Provincial Key Laboratory of Atmospheric Environment and Pollution Control, South China University of Technology, Guangzhou 510006, P.R. China;

[f] Department of Chemistry, University of Connecticut, Storrs, Connecticut 06269, USA.

* Corresponding author. E-mail: liangxl@gig.ac.cn (X. L. LIANG).

## Experimental section

### 1. Materials and methods

*1.1. Catalyst preparation.*

Ca-substituted $LaCoO_3$ catalysts were prepared by a one-pot sol-gel method. $La(NO_3)_3 \cdot 6H_2O$, $Ca(NO_3)_2 \cdot 4H_2O$, $Co(NO_3)_3 \cdot 6H_2O$, and $C_6H_8O_7 \cdot H_2O$ (CA) were dissolved in a mixed solvent ($V_{H_2O}$:$V_{Ethanol}$ = 2:1) with a mole ratio of $La^{3+}$:$Ca^{2+}$:$Co^{3+}$:CA equal to 1-*x*:*x*:1:2. The obtained solution was stirred for 30 min, sonicated for 10 min at room temperature and heated to 80 °C until a gel was formed, followed by evaporating water under vacuum at 90 °C to obtain the precursor. Then, the precursor was milled and calcined at 700 °C for 5 h with a heating rate of 5 °C $min^{-1}$. The obtained solid was ground and sieved to 40-60 mesh. Ca-substituted $LaCoO_3$ catalysts were denoted as Ca-*x*. It is noteworthy that for Ca-0.4, additional reflections of CaO are observed (Fig. S1), suggesting that CaO impurities are distributed on the $LaCoO_3$ surface without being incorporated into the perovskite structure. Thus, this study focused on the Ca-*x* samples with *x* in the range of 0-0.3.

*1.2. Catalyst characterization.*

Powder X-ray diffraction (PXRD) patterns were recorded between 20° and 80° (2$\theta$) at a step of 1° $min^{-1}$ on a Bruker D8 advance diffractometer with Cu *K*$\alpha$ radiation (40 kV and 40 mA). The crystalline size was determined using Scherrer's equation. Transmission electron microscopy (TEM) and electron energy loss spectroscopy

(EELS) analyses were performed on an FEI Talos F200S with a spherical aberration corrector. All the particles were dispersed in ethanol on a carbon-coated copper grid. To analyze the valence state of cobalt, the background was subtracted from the EELS spectra, and the multiple scattering effect was removed using the Fourier ratio deconvolution technique.[1] Specific surface area measurements were carried out by the BET method on the basis of $N_2$ physisorption capacity at 77 K on a Micromeritics ASAP 2020 instrument. Fourier transform infrared spectra (FTIR) were recorded on a Bruker Vector 70 infrared spectrometer using a KBr substrate. The hydrogen temperature programmed reduction ($H_2$-TPR) was evaluated in the range of 30-800 °C at a heating rate of 10 °C $min^{-1}$. The 50.0 mg sample was preheated at 250 °C under Ar for 30 min. The $H_2$ consumption was estimated by the curve-fitting method using a standard CuO sample for calibration. The temperature-programmed desorption of oxygen ($O_2$-TPD) was carried out on a Beijing Builder PCA-1200 chemisorption instrument equipped with a TCD detector and evaluated in the range of 40-550 °C at a heating rate of 10 °C $min^{-1}$ under He flow. A 100.0 mg sample was pretreated at 250 °C for 1 h and cooled to 40 °C under $O_2$. The core level (CL) spectra and valence band (VB) spectra of the samples were investigated by X-ray photoelectron spectroscopy (XPS) using a Thermo Fisher K-Alpha instrument equipped with an Al Kα source (10 mA, 14 kV) that was operated at 1486.8 eV. The pass energy for a full spectrum was 50 eV for single element analysis and 30 eV for the valence band spectra. Charge shifting was corrected by adjusting the binding

energy of C 1s to 284.8 eV. The O p band center relative to the Femi level ($E_F$) can be obtained by VB spectra through Gaussian-Lorentzian fitting. All the spectra were corrected for the background using the Shirley approach.

*1.3. Catalytic experiment.*

The catalytic oxidation of toluene by Ca-*x* was performed in a conventional fixed-bed reactor in the temperature range of 100-400 °C under atmospheric pressure. A 100.0 mg of catalyst was loaded in a quartz tube reactor (i.d. = 6 mm) supported by a porous quartz plate. Gaseous toluene was generated by flowing $N_2$ into liquid toluene at 0 °C. The inlet gas was composed of 1000 ppm toluene and 20 vol% oxygen balanced by $N_2$. The total flow rate was 100 mL $min^{-1}$, corresponding to a gas hourly space velocity (GHSV) of 60 000 $cm^3$ $g^{-1}$ $h^{-1}$. The toluene oxidation efficiency was expressed by the $CO_2$ generation efficiency (Eq. (1)):

$$CO_2 \text{ generation efficiency} = C_{CO_2}/C^*_{CO_2} \times 100\% \quad (1)$$

where $C_{CO_2}$ and $C^*_{CO_2}$ are the $CO_2$ concentrations in the effluent at different temperatures and when toluene was completely oxidized to $CO_2$, respectively. The concentration of $CO_2$ in the effluent was analyzed online by a nondispersive infrared $CO_2$ analyzer (Beijing Huayun GXH-3010E).

*1.4. The specific reaction rate constant ($R_s$) calculation.*

The reaction rate (*r*, μmol $g^{-1}$ $s^{-1}$) was defined as the number of toluene molecules

oxidized over catalysts per second per gram (Eq. (2)).

$$r = (C_{toluene} \times X_{toluene} \times V_{gas})/m \quad (2)$$

where $m$ is the catalyst mass (g), $C_{toluene}$ is the concentration of toluene in the gas mixture (μmol $mL^{-1}$), $X_{toluene}$ is the conversion of toluene (%), and $V_{gas}$ is the total flow rate (mL $s^{-1}$).

To exclude the influence of surface area, the specific reaction rate constant ($R_s$) of $LaCoO_3$-based catalysts was calculated (Eq. (3)).

$$R_s = r/S \quad (3)$$

where S is the specific surface area ($m^2$ $g^{-1}$).

*1.5. Details for activation energy calculation.*

The discrepancy in the catalytic activity of the as-prepared catalysts was further manifested by the apparent activation energy ($E_a$, kJ $mol^{-1}$), which was evaluated by Arrhenius plots (Eq. (4)).

$$r = A \exp(-E_a/RT) [O_2]^a [toluene]^b \quad (4)$$

where $r$ is reaction rate of toluene (μmol $g^{-1}$ $s^{-1}$); A is pre-exponential factor, R is molar gas constant, 8.314 J $mol^{-1}$ $K^{-1}$; and a and b were the reaction orders for $O_2$ and toluene, respectively.

According to previous study,[2] the oxidation of VOCs over metal oxides in the presence of excess oxygen follows first-order and zero-order kinetics with respect to the concentrations ($C$, μmol $g^{-1}$) of toluene and oxygen, respectively. Thus, in this

study, the catalytic oxidation of toluene by excess oxygen obeyed the first-order kinetics towards the toluene concentration ($C$, umol $g^{-1}$, Eq. (5)).

$$r = kC = \mathrm{A}\ \exp(-E\mathrm{a}/\mathrm{R}T)\ C \qquad (5)$$

where $k$ is the kinetic rate constant ($s^{-1}$), calculated by the reaction rates and toluene concentration. Taking the natural log of both sides, Eq. (5) can be transformed to Eq. (6).

$$lnk = ln(r/C) = -\ Ea/RT + lnA \qquad (6)$$

The activation energy ($E_a$) was calculated from the fitted least squares of Eq. (6).

*1.6. Details for DFT calculations.*

To determine the relationship between the electron structure and catalytic performance of substituted $LaCoO_3$ perovskite oxides, first-principles DFT+U calculations were carried out on the oxygen p states for all Ca-$x$ ($x$ = 0, 0.1, 0.2, 0.3). We employed the Vienna Ab initio Simulation Package (VASP) [3, 4] to perform all density functional theory (DFT) calculations within the generalized gradient approximation (GGA) using the Perdew-Burke-Ernzerhof (PBE) formulation.[5] The GGA + U calculations were performed using the model proposed by Dudarev et al. [6] with $U_{eff}$ ($U_{eff}$ = Coulomb U – exchange J) values of 3.3 eV for Co metals. For all compositions, the lattice constants and ion positions were first fully relaxed. Then, density of states (DOS) calculations was performed on the fully relaxed stoichiometric structures. The projected augmented wave (PAW) potential [7, 8] was selected to

describe the ionic cores taking valence electrons into account using a plane wave basis set with a kinetic energy cutoff of 520 eV. The density of the k-mesh grids for Brillouin zone sampling was set as 0.04×2$\pi$/Å. Partial occupancies of the Kohn-Sham orbitals were allowed using the Gaussian smearing method and a width of 0.05 eV. The electronic energy was considered self-consistent when the energy change was smaller than $10^{-6}$ eV. The geometry optimization was considered convergent when the force on each atom was smaller than 0.02 eV/Å. For rhombohedral-type perovskites, a hexa-rhombohedral unit (6 × $ABO_3$) was used, and the γ-centered k-point mesh for DOS calculation was set to be 10 × 10 × 4. The formation enthalpy of O vacancies in bulk Ca-*x* was calculated using Eq. (7):

$$E_f = E_{vac} + 1/2E_{O_2} - E_{pristine} \quad (7)$$

where $E_f$ is the formation enthalpy of the oxygen vacancy, $E_{vac}$ is the total energy of the system with a single oxygen vacancy, $E_{O_2}$ is the free energy of the $O_2$ molecule, and $E_{pristine}$ is the total energy of the system without any defect.

The adsorption energies of $O_2$ molecules on Ca-*x* (110) surfaces were calculated according to Eq. (8):

$$E_{ads} = E_{tot} - E_{O_2} - E_{slab} \quad (8)$$

where $E_{ads}$ is the adsorption energy of the $O_2$ molecule, $E_{tot}$ is the total energy of the slab model after $O_2$ adsorption, $E_{O_2}$ is the free energy of the $O_2$ molecule, and $E_{pristine}$ is the total energy of a pristine slab model (without $O_2$ adsorption).

The O p band center were computed by taking the weighted mean energy of the

projected density of states of O p states (both occupied and unoccupied states) relative to the Fermi level. The O p band center relative to the $E_F$ can be calculated by Eq. (9).[9, 10]

$$\text{O p band center} = \frac{\int_{-\infty}^{\infty} x\rho(x)dx}{\int_{-\infty}^{\infty} \rho(x)dx} \quad (9)$$

where $x$ and $\rho(x)$ are the energy and density of states, respectively.

**Table captions**

**Table S1.** Lattice parameter ($a_0$), crystal size, surface area and porosity of Ca-*x* samples.

**Table S2.** Chemical composition and surface element distribution of Ca-*x* catalysts.

**Table S3.** The catalytic activity (T10, T50, and T90), specific reaction rate constant ($R_s$), kinetic rate constant ($k$), and activation energy ($E_a$) of the Ca-*x* catalysts for toluene oxidation.

**Table S4.** Summary of previous research papers on toluene combustion over cobalt related catalysts.

**Table S5.** Surface oxygen species, the oxygen desorption amounts and initial reduction temperature of Ca-*x* catalysts.

**Table S1.** Lattice parameter ($a_0$), crystal size, surface area and porosity of Ca-*x* samples.

| Samples | $a_0$/Å | [a]crystal size/nm | Surface area/$m^2\ g^{-1}$ | Pore volume/$cm^3\ g^{-1}$ | Pore size/nm |
|---|---|---|---|---|---|
| Ca-0 | 5.443 | 24.5 | 7.2 | 0.024 | 15.8 |
| Ca-0.1 | 5.422 | 20.9 | 13.7 | 0.080 | 24.8 |
| Ca-0.2 | 5.417 | 18.2 | 19.1 | 0.087 | 18.7 |
| Ca-0.3 | 5.405 | 16.2 | 17.8 | 0.077 | 18.1 |

[a] Calculated from XRD results with Scherrer equation: $D = k\lambda/(\beta\cos\theta)$ applied to the (024) diffraction peak. D is crystal size, λ is the X-ray wavelength (0.154 nm), β is the FWHM of the XRD peak, and k is the shape factor and usually taken as about 0.89.

**Table S2.** Chemical composition and surface element distribution of Ca-*x* catalysts.

| Samples | *n*(La)/*n*(La+Ca+Co)[a] | *n*(Co)/*n*(La+Ca+Co)[b] | *n*(Ca)/*n*(La+Ca+Co)[c] | *n*(Ca)/*n*(La+Ca+Co)[d] | *n*(Ca)/*n*(La+Ca+Co)[e] |
|---|---|---|---|---|---|
| Ca-0 | 0.49 | 0.51 | 0 | 0 | 0 |
| Ca-0.1 | 0.45 | 0.50 | 0.05 | 0.05 | 0.05 |
| Ca-0.2 | 0.41 | 0.50 | 0.09 | 0.10 | 0.10 |
| Ca-0.3 | 0.36 | 0.50 | 0.14 | 0.19 | 0.15 |

a, b, c: Element atomic ratio in bulk analyzed by ICP-AES; d: Element atomic ratio on surface analyzed by XPS; e: Theoretical mole ratio of Ca-*x* samples.

**Table S3.** The catalytic activity (T10, T50, and T90), specific reaction rate constant ($R_s$), kinetic rate constant ($k$), and activation energy ($E_a$) of the Ca-$x$ catalysts for toluene oxidation.

| Samples | Toluene oxidation/$^{o}$C | | | $^{a}R_s$/μmol $s^{-1}$ $m^2$ | $^{a}k$/$s^{-1}$ | $E_a$/kJ $mol^{-1}$ |
|---|---|---|---|---|---|---|
| | $T_{10\%}$ | $T_{50\%}$ | $T_{90\%}$ | | | |
| Ca-0 | 228 | 260 | 280 | 0.094 | 0.028 | 52.9 |
| Ca-0.1 | 205 | 232 | 241 | 0.112 | 0.033 | 43.8 |
| Ca-0.2 | 190 | 212 | 220 | 0.135 | 0.077 | 40.0 |
| Ca-0.3 | 198 | 225 | 232 | 0.118 | 0.051 | 42.2 |

[a] Reaction condition: catalyst = 100 mg, toluene = 1000 ppm, $O_2$ = 20%, and $N_2$ balance, gas rate = 100 mL $min^{-1}$, and temperature = 200 $^{o}$C.

**Table S4.** Summary of previous research papers on toluene combustion over cobalt related catalysts.

| Catalysts | Surface area/$m^2g^{-1}$ | Concentration /ppm | GHSV /$mLg^{-1}.h^{-1}$ | T50 /°C | T90 /°C | References |
|---|---|---|---|---|---|---|
| $Co_3O_4$ | 51.7 | 1000 | 20000 | 195 | 215 | [11] |
| CoMn0.5 | 249 | 1200 | 60000 | 271 | 311 | [12] |
| Pd/Co3AlO | 93 | 800 | 30000 | 220 | 230 | [13] |
| Co30Ce | 33 | 1000 | 36000 | 233 | 260 | [14] |
| Au/$Co_3O_4$ | 1.6 | 146 | 14690 | 200 | | [15] |
| Ru/$Co_3O_4$-MOF | 80 | 1000 | 60000 | 231 | 238 | [16] |
| Montmorillonite pillared by $Co_3O_4$ | 53 | 1000 | 30000 | 284 | 297 | [17] |
| CoAlO | 88.6 | 2000 | 60000 | 307 | 319 | [18] |
| Ag–CoAlO | 69.5 | 2000 | 60000 | 293 | 300 | [18] |
| Pt–CoAlO | 81.1 | 2000 | 60000 | 282 | 289 | [18] |
| Pd–CoAlO | 51.8 | 2000 | 60000 | 222 | 226 | [18] |
| [a]CoCe-P | 89 | 1000 | 60000 | 212 | 230 | [19] |
| [b]$Co_3O_4$-C | 83.1 | 1000 | 48000 | 240 | 248 | [20] |
| [c]$Co_3O_4$-P | 58.8 | 1000 | 48000 | 243 | 254 | [20] |
| [d]$Co_3O_4$-N | 25.9 | 1000 | 48000 | 250 | 259 | [20] |
| 3D-$Co_3O_4$ | 84.6 | 1000 | 48000 | 229 | 238 | [21] |
| 2D-$Co_3O_4$ | 24.9 | 1000 | 48000 | 242 | 249 | [21] |
| 1D-$Co_3O_4$ | 24.9 | 1000 | 48000 | 245 | 257 | [21] |
| [e]$Co_3O_4$/3DOM-ESFO | 24.1 | 1000 | 20000 | 251 | 269 | [22] |
| $LaCoO_3$/SBA-15 | 353 | 1000 | 20000 | 284 | 310 | [23] |
| [f]$Co_3O_4$/3DOM-LSCO | 29.7 | 1000 | 20000 | 210 | 227 | [24] |
| $La_{0.6}Sr_{0.4}Co_{0.9}Fe_{0.1}O_3$ | 21 | 1000 | 20000 | 220 | 239 | [25] |
| [g]La–Co CX 1:2 | 92 | 266 | 60000 | 307 | 350 | [26] |
| [h]La–Co EM 1:2 | 68 | 266 | 60000 | 258 | 283 | [26] |
| [i]LCO-1 | 5.81 | 1000 | 60000 | 206 | 223 | [27] |
| Spherical $LaCoO_3$ | 20.7 | 1000 | 20000 | 220 | 237 | [28] |
| Au/3 DOM $LaCoO_3$ | 26.8 | 1000 | 20000 | 193 | 214 | [29] |
| [f]Ag/LCO-450 | 11.9 | 1000 | 60000 | 239 | 279 | [30] |
| $La_{0.98}Ag_{0.02}CoO_3$ | 7.5 | 1000 | 60000 | 225 | 251 | [30] |
| $La_{0.8}Ca_{0.02}CoO_3$ | 19.1 | 1000 | 60000 | 212 | 220 | This study |

[a] CoCe-P, CoOx/$CeO_2$ nanoparticles; [b] $Co_3O_4$-C, 3D hierarchical cubes-stacked $Co_3O_4$ microspheres; [c] $Co_3O_4$-P, 3D hierarchical plates-stacked $Co_3O_4$ flower; [d] Co3O4-N, 3D hierarchical needles-stacked $Co_3O_4$ two spheres with an urchin-like structure. [e] $Co_3O_4$/3DOM-ESFO, 3DOM $Co_3O_4$/$Eu_{0.6}Sr_{0.4}FeO_3$. [f] $Co_3O_4$/3DOM-LSCO, $Co_3O_4$/3DOM $La_{0.6}Sr_{0.4}CoO_3$. [g-h] La-Co mixed oxides are prepared by evaporation method (EM) and

exotemplating method (EX). [i]LCO-1, acetic acid treated LCO for 1 h. [j]Ag/LCO-450, Impregnation method synthesized $Ag/LaCoO_3$ and calcined at 450 °C.

**Table S5.** Surface oxygen species, the oxygen desorption amounts and initial reduction temperature of Ca-*x* catalysts.

| Samples | Oxygen species [a] | | | $O_{ads}/O_{lat}$ [a] | Desorption amount/μmol $g^{-1}$ [b] | | Initial reduction temperature/°C |
|---|---|---|---|---|---|---|---|
| | $O^{2-}$ | $O^{-}$, $O_2^{2-}$ | $OH^{-}$, $CO_3^{2-}$ | | 150-300 °C | 300-500 °C | |
| Ca-0 | 41.9 | 55.5 | 3.6 | 1.2 | 92.4 | 134.0 | 226 |
| Ca-0.1 | 42.4 | 54.0 | 3.6 | 1.3 | 165.3 | 424.6 | 233 |
| Ca-0.2 | 37.8 | 60.7 | 1.5 | 1.7 | 251.6 | 582.7 | 188 |
| Ca-0.3 | 36.3 | 60.4 | 3.3 | 1.6 | 217.6 | 640.7 | 205 |

a: obtained from XPS analysis. b: obtained from TPD analysis.

**Figure captions**

**Fig. S1.** PXRD patterns of Ca-0.4 samples and the standard card of perovskite-type $LaCoO_3$ (JCPDS: 25-1060).

**Fig. S2.** PXRD patterns of Ca-*x* samples and the standard card of perovskite-type $LaCoO_3$ (JCPDS: 25-1060).

**Fig. S3.** $N_2$ adsorption-desorption isotherms of Ca-*x* samples.

**Fig. S4.** SEM (a) and Ca mapping image (b) of Ca-0.3.

**Fig. S5.** SEM images of Ca-0 (a), Ca-0.1 (b), Ca-0.2 (c), and Ca-0.3 (d).

**Fig. S6.** Co 2p (a) and O 1s (b) XPS of Ca-*x* catalysts.

**Fig. S7.** Electron spin resonance spectra (a) and formation enthalpy of $O_v$ (b) spectra of Ca-*x* catalysts.

**Fig. S8.** VB spectra of Ca-*x* samples.

**Fig. S9.** The relationship between the $O_{ads}/O_{lat}$ (a), $O_\alpha$ (b), initial reduction temperature (c) and the toluene conversion rates ($R_s$) of Ca-*x* catalysts.

**Fig. S10.** The relationship between O p band center and the initial reduction temperature (a), $O_\alpha$ (b) of Ca-*x* catalysts.

**Fig. S11.** The relationship between the O p band center (VB spectra) and the toluene conversion rates ($R_s$) of Ca-*x* catalysts.

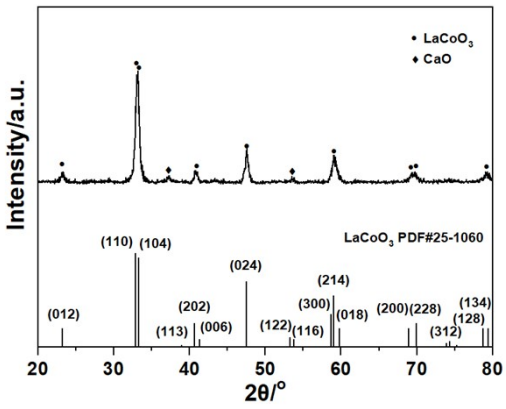


215

**Fig. S1.** PXRD patterns of Ca-0.4 samples and the standard card of perovskite-type $LaCoO_3$ (JCPDS: 25-1060).

For Ca-0.4, in addition to the reflections of $LaCoO_3$ perovskite, additional reflections 220 of CaO are observed at $2\theta = 37.3^{o}$ and $53.6^{o}$ (Fig. S1).

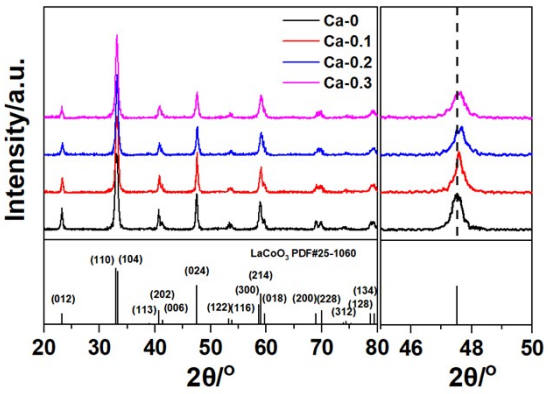


**Fig. S2.** PXRD patterns of Ca-*x* samples and the standard card of perovskite-type $LaCoO_3$ (JCPDS: 25-1060).

The XRD patterns of Ca-*x* correspond to the standard card of hexagonal $LaCoO_3$ (JCPDS 25-1060) (Fig. S2).[31] With increasing Ca content, the intensities of all the reflections increase, and the strong reflection (024) at $2\theta = 47.6^{o}$ gradually shifts to a high angle. The $a_0$ obviously decreases from 5.443 to 5.405 Å (Table S1) due to the smaller radius of $Ca^{2+}$ (1.118 Å) than $La^{3+}$ (1.122 Å).[32] This confirms the successful incorporation of Ca in perovskite $LaCoO_3$. According to Scheler's equation, the crystal size gradually decreases from 24.5 to 16.2 nm (Table S1). Thus, with the increase of Ca substitution, the particle size decreases, which increases the specific surface area. Similar phenomenon is also found in the study on $LaFeO_3$ with Ca substitution [33].

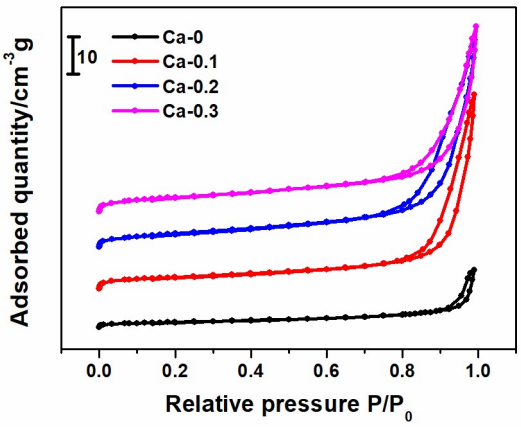


**Fig. S3.** $N_2$ adsorption-desorption isotherms of Ca-*x* samples.

240

The $N_2$ adsorption-desorption isotherms are typical of type IV with an H3 hysteresis loop (Fig. S3). The high onsets of $p/p_0$ (0.8-1.0) of hysteresis loops are related to the macropores and large mesopores in the agglomerates.[34] According to the SEM observation, Ca substitution makes $LaCoO_3$ generate more stacked macropores

245 and mesopores. This results in an increase in the specific surface area (SSA) from 7.2 to 19.1 $m^2\ g^{-1}$, as well as an increase in the pore volume from 0.024 to 0.077-0.087 $cm^3\ g^{-1}$ (Table S1), which facilitates contact between VOC molecules and the active sites inside the pores.

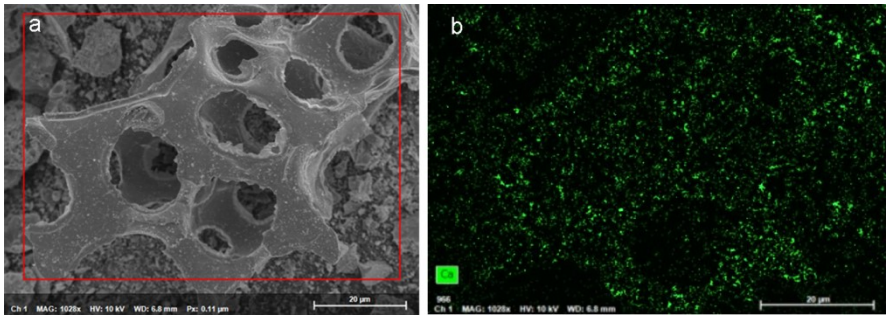


**Fig. S4.** SEM (a) and Ca mapping image (b) of Ca-0.3.

The Ca mapping image of Ca-0.3 showed that Ca is enriched on the surface of $LaCoO_3$ (Fig. S4). This suggests that at a high substitution level, Ca prefers to be enriched on the surface of $LaCoO_3$. The molar ratios in the bulk phase, i.e., n(La)/n(La+Ca+Co), n(Ca)/n(La+Ca+Co) and n(Co)/n(La+Ca+Co), are close to those of the theoretical stoichiometry (Table S2). However, different from Ca-0.1 and Ca-0.2, the ratio of surface n(Ca)/n(La+Ca+Co) (0.19) on Ca-0.3 is obviously higher than that in the bulk (0.14). This suggests that at a high substitution level, Ca prefers to be enriched on the surface, which is further confirmed by Ca mapping of the SEM image (Fig. S4). This is probably ascribed to the difference in both ionic radii and charge between $Ca^{2+}$ (1.118 Å) and $La^{3+}$ (1.122 Å), [32] which leads to the outward diffusion of $Ca^{2+}$ during crystal growth.

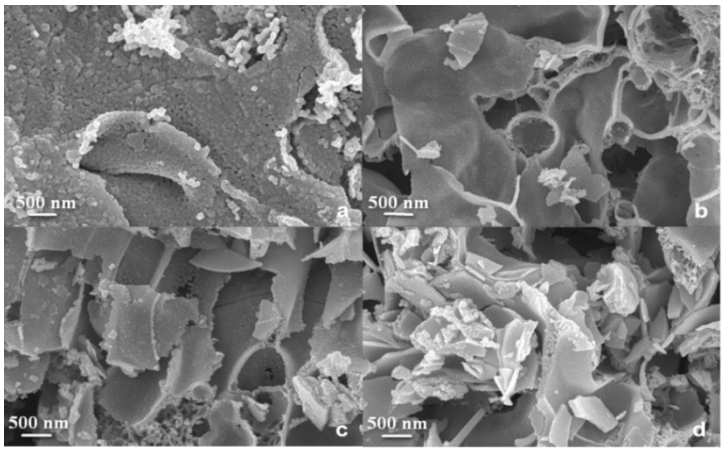


**Fig. S5.** SEM images of Ca-0 (a), Ca-0.1 (b), Ca-0.2 (c), and Ca-0.3 (d).

The effects of Ca substitution treatment on the morphology and microstructure of $LaCoO_3$ was observed by SEM (Fig. S5). $LaCoO_3$ displays the rough surface (Fig. S5a), due to the larger size of the spherical particles (ca. 30 nm). With the increase of Ca displacement, the particle size decreases, making the surface of the sheet smoother. In addition, Ca substitution leads to the formation of more stacked mesoporous and macroporous between the particles (Fig. S3, Figs. S5b and c). Compared to the Ca-0.1 and Ca-0.2, many small fragments are blocked in the accumulation hole in Ca-0.3 (Figs. S5d), resulting in a slight decrease in the specific surface area. According to the SEM and BET, Ca substitution makes $LaCoO_3$ generate more stacked macropores and mesopores.

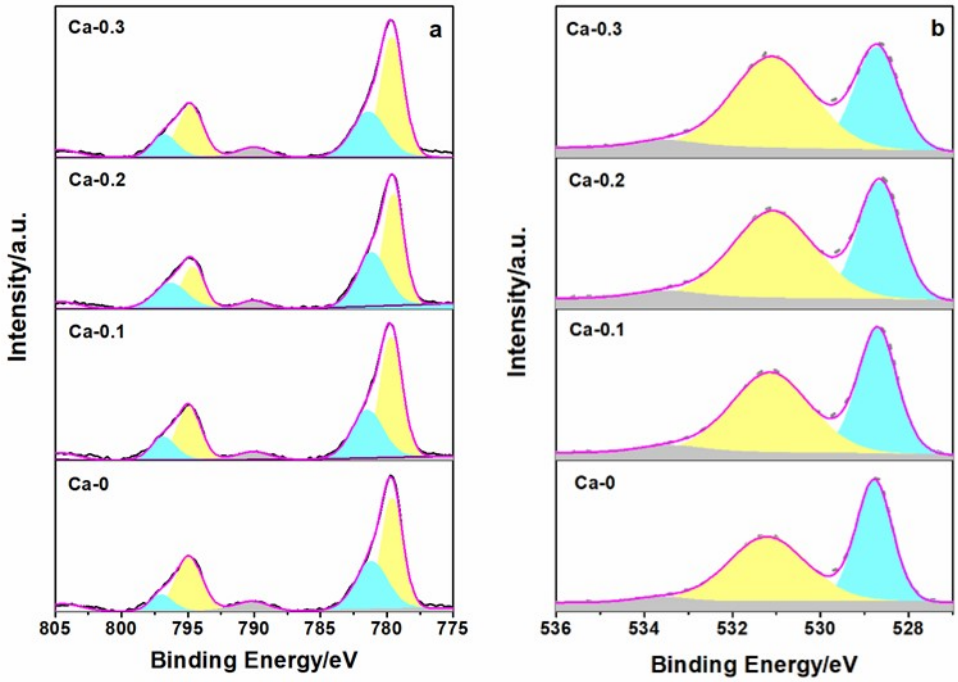


**Fig. S6.** Co 2p (a) and O 1s (b) XPS of Ca-*x* catalysts.

The variation in Co valence was further analyzed by XPS. The spectra show Co $2p_{3/2}$ and Co $2p_{1/2}$ binding energies located at 780.1 and 795.1 eV, respectively (Fig. S6a), which are deconvoluted into three components, i.e., $Co^{2+}$, $Co^{3+}$, and the shake-up peak.[29, 35] The peaks at approximately 779.6 and 794.9 eV are assigned to $Co^{2+}$, while the peaks at approximately 781.2 and 797.1 eV correspond to $Co^{3+}$.[36, 37] Based on the spectral area, $Co^{2+}/Co^{3+}$ increases in the order of Ca-0 (0.30) < Ca-0.1 (0.33) < Ca-0.3 (0.35) < Ca-0.2 (0.39). As the substitution of $La^{3+}$ (1.122 Å) by $Ca^{2+}$ (1.118 Å) decreases $a_0$, this promotes the reduction of $Co^{3+}$ (0.68 Å) to $Co^{2+}$ (0.79 Å) to compensate for the lattice contraction.[38]

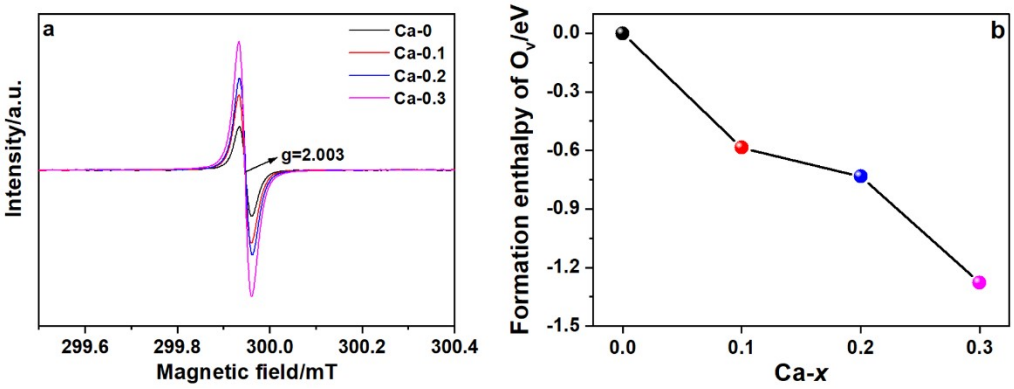


**Fig. S7.** The electron spin resonance spectra (a) and formation enthalpy of $O_v$ (b) spectra of Ca-*x* catalysts.

This is identified by electron spin resonance (ESR) spectra displaying a symmetrical peak at g = 2.003, arising from the unpaired electrons at oxygen vacancies (Fig. S7a).[39, 40] With increasing Ca substitution, the peak intensity gradually increases. Thus, among Ca-*x*, Ca-0.3 with the highest intensity has the most $O_v$.[39] This is also interpreted in terms of the enthalpy $E_f$ of $O_v$ (-1.5-0 eV) formation calculated by DFT, which decreases with increasing Ca substitution (Fig. S7b).

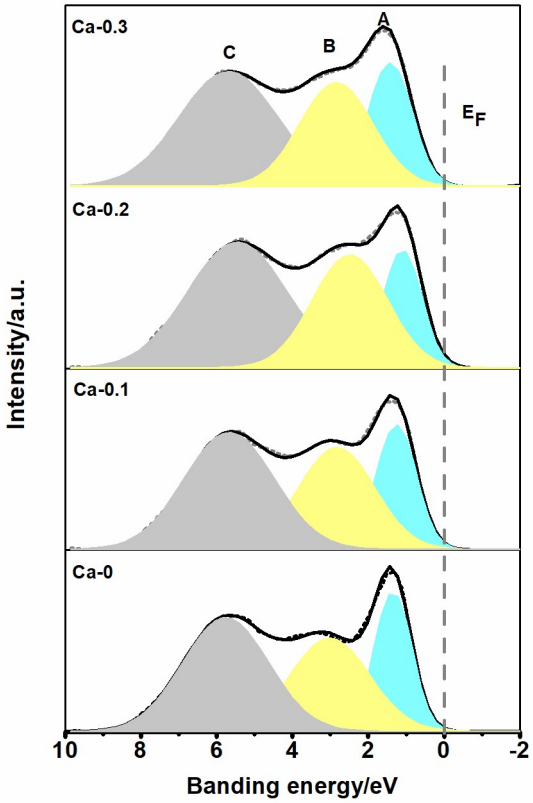


**Fig. S8.** VB spectra of Ca-*x* samples.

In this study, the O p band center relative to the $E_F$ of Ca-*x* samples were calculated by VB spectra.[35, 41] The obtained asymmetrical spectra are fitted by Gaussian-Lorentzian and deconvoluted into three symmetrical peaks of A, B, and C at approximately 1.2, 3.0, and 5.8 eV, respectively (Fig. S8). Peaks A and C are attributed to the Co 3d state, while peak B is mainly attributed to the O 2p state.[35] Hence, the binding energy of O 2p is the position of the O p band center to the Fermi level.[35] For Ca-0, Ca-0.1, Ca-0.2 and Ca-0.3, the O p band center are -3.11, -2.9, -2.57, and -2.85 eV, respectively. The position of the O p band center gradually approaches the Fermi level with increasing Ca substitution from $x$=0 to $x$=0.2 but changes the Fermi level at higher Ca substitution at $x$=0.3. Since the relative position of the O p band determines the redox activity of cations and anions,[42, 43] Ca-*x* catalysts with lower energy states of O than Co indicate the strong binding of adsorbates to cations and relatively inactive lattice oxygen.[44]

According to Grimaud et al., study, [45] the O p band center relative to the Fermi level of Co-based catalysts is linearly increase with increasing the valence state of cobalt. The average valence state of cobalt was analyzed by the XPS Co 2*p* spectra (Fig. S6a), which displays negative correlation to the binding energy difference between the Co 2*p*3/2 and Co 2*p*1/2. For example, the reported values for CoO (cobalt valence=2) and $Co_3O_4$ (cobalt valence =2.67) are 15.5 eV and 15.3 eV, respectively. [46] For Ca-*x*, the relevant to the binding energy difference between the Co 2*p*3/2 and Co 2*p*1/2 in Ca-0, Ca-0.1, Ca-0.2 and Ca-0.3 were 15.21, 15.11, 14.99, and 15.02 eV, respectively. Thus, the average valence state of cobalt in Ca-0, Ca-0.1, Ca-0.2 and Ca-0.3 were determined to be +2.98, +3.31, +3.71, and +3.61, respectively, which increases with the Ca substitution from *x*=0 to *x*=0.2, but then slightly decreases at a higher Ca substitution of *x*=0.3. Thus, with the increase in Ca substitution from *x*=0 to *x*=0.2, the position gradually approaches $E_F$ but then slightly deviates at a higher Ca substitution of *x*=0.3.

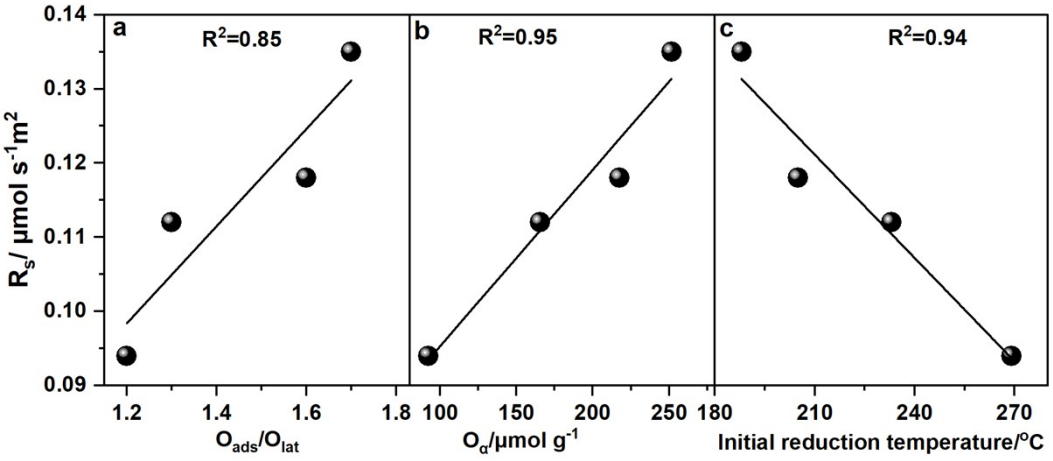


**Fig. S9.** The relationship between the $O_{ads}/O_{lat}$ (a), $O_{\alpha}$ (b), initial reduction temperature (c) and the toluene conversion rates ($R_s$) of Ca-*x* catalysts.

$H_2$-TPR can provide some information, such as the reducibility of the metallic ions, the activity of the surface and lattice oxygen ions, and the stability of the catalysts. During $H_2$-TPR process, the metal ions with high valence are reduced to the ions with low valence or metal atoms by $H_2$. The surface oxygen ions and the lattice oxygen ions also participate in the reduction reaction.[47] Therefore, the reduction peaks reflect not only the reducibility of the metal ions but also the activity of oxygen species. The various oxygen active species of the catalyst also can be detected by $O_2$-TPD.[37] To illustrate the improvement mechanism, the variation in the above physico-chemical properties is linked to the catalytic activity of Ca-*x* (Fig. S9). A good relationship is found between $R_s$ and $O_{ads}/O_{lat}$ ($R^2$=0.85), $O_{\alpha}$ ($R^2$=0.95) and the initial reduction temperature of oxygen ($R^2$=0.94). This indicates that these properties are the vital factors that determine the effects of Ca substitution on the catalytic activity of $LaCoO_3$. Due to the generation of vacancies by the inequivalent substitution of $La^{3+}$ by $Co^{2+}$, Ca substitution increases the number of surface oxygen species (e.g., $O_2^-$, $O_2^{2-}$ or $O^-$), as evidenced by the increase in $O_{ads}/O_{lat}$ and $O_{\alpha}$. The surface oxygen species are strong electrophilic reactants and attack toluene in the region of its highest electron density, leading to its oxidation. On the other hand, Ca substitution lowers

the reduction temperature of oxygen, making its activation easier. Both variations enhance the catalytic activity of Ca-*x* in toluene oxidation.

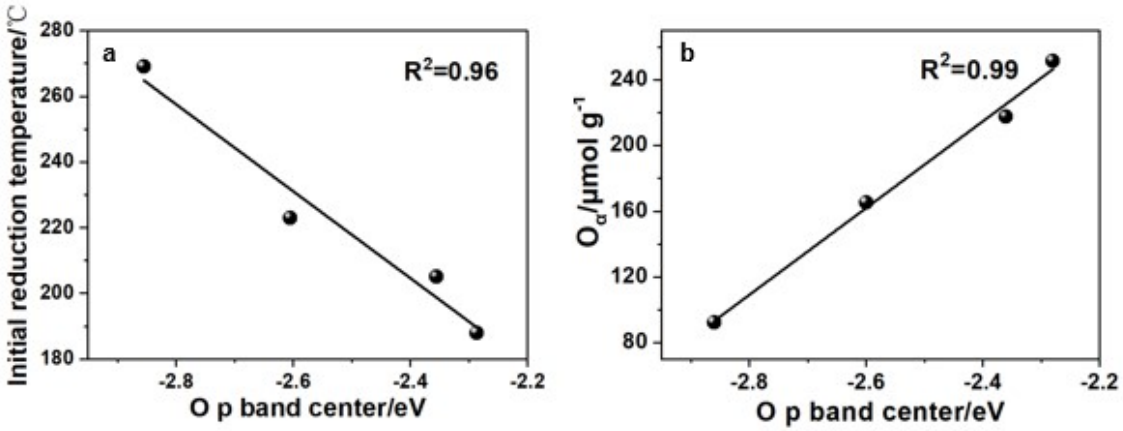


**Fig. S10.** The relationship between O p band center and the initial reduction temperature (a), $O_\alpha$ (b) of Ca-x catalysts.

The O p band center of Ca-x showed a good correlation with the initial reduction temperature ($R^2$=0.96, Fig. S10a) and $O_\alpha$ ($R^2$=0.99, Fig. S10b). This indicates that the O p band center greatly affects the reducibility and active oxygen species. The O p band center dominates the strength of metal-to-oxygen bonds.[48] The lower the O p band center is, the weaker the metal-oxide bond strength, which accordingly leads to easier reduction. Thus, among Ca-*x*, Ca-0.2 with the lowest O p band center displays the lowest initial reduction temperature. In contrast, for other Ca-*x*, a higher initial reduction temperature is observed, as its O p band center is far from EF. Similar to the initial reduction temperature, the activation and release of oxygen also depend on the metal-oxide bonds.[49] The release of oxygen is easier when the O p band center is closer to the $E_F$. Thus, for Ca-0.2 with the lowest O p band center, the $O_\alpha$ content is the highest. Due to the aforementioned finding that reducibility as well as surface $Co^{2+}$ and oxygen are vital for the catalytic activity of Ca-*x*, it is promising to utilize the O p band center to predict the variation in activity. This is proven by the good correlation between $R_s$ and O p band center obtained by DFT ($R^2$=0.92, Fig. 4d) and VB spectra ($R^2$=0.97, Fig. S11). The ‘‘volcano’’ type variation of the Co-oxide bond strength, diagnosed by the O p band center, accounts for the optimal catalytic activity of Ca-0.2 in toluene decomposition.

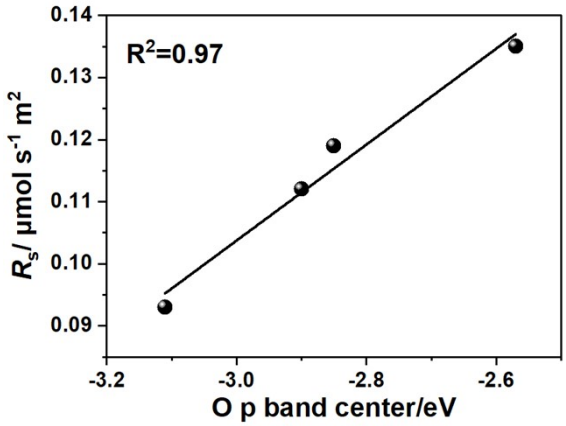


380 **Fig. S11.** The relationship between the O p band center (VB spectra) and the toluene conversion rates ($R_s$) of Ca-*x* catalysts.

## References


1. D. H. Pearson, C. C. Ahn and B. Fultz, *Phys. Rev. B, Condens. Matter.*, 1993, **47**, 8471-8478.
2. M. Alifanti, M. Florea, S. Somacescu and V. I. Parvulescu, *Appl. Catal. B-Environ.*, 2005, **60**, 33-39.
3. G. Kresse and J. Furthmüller, *Phys. Rev. B,* 1996, **11169-11186**.
4. J. B. Neaton and N. W. Ashcroft, *Nature*, 1999, **400**, 141-144.
5. J. P. Perdew, K. Burke and M. Ernzerhof, *Phys. Rev. Lett.*, 1998, **77**, 3865-3868.
6. S. L. Dudarev, G. A. Botton, S. Y. Savrasov, C. J. Humphreys and A. P. Sutton, *Phys. Rev. B,* 1998, **57**, 1505-1509.
7. G. Kresse and D. Joubert, *Phys. Rev. B*, 1999, **59**, 1758-1775.
8. P. E. Blochl, *Phys. Rev. B, Condens. Matter.*, 1994, **50**, 17953-17979.
9. J. N. Rskov, F. Studt, F. Abildpedersen and T. Bligaard, *Wiley*, 2015.
10. T. Wang, C. Zhang, J. Wang, H. Li and Z. J. Xu, *J. Catal.*, 2020, **390**, 1-11.
11. G. M. Bai, H. X. Dai, J. G. Deng, Y. X. Liu, F. Wang, Z. X. Zhao, W. G. Qiu and C. T. Au, *Appl. Catal. A-Gen.*, 2013, **450**, 42-49.
12. D. A. Aguilera, A. Perez, R. Molina and S. Moreno, *Appl. Catal. B-Environ.*, 2011, **104**, 144-150.
13. P. Li, C. He, J. Cheng, C. Y. Ma, B. J. Dou and Z. P. Hao, *Appl. Catal. B-Environ.*, 2011, **101**, 570-579.
14. L. F. Liotta, M. Ousmane, G. Di Carlo, G. Pantaleo, G. Deganello, A. Boreave and A. Giroir-Fendler, *Catal. Lett.*, 2009, **127**, 270-276.
15. H. J. Wu, L. D. Wang, Z. Y. Shen and J. H. Zhao, *J. Mol. Catal. A-Chem.*, 2011, **351**, 188-195.
16. X. L. Liu, J. Wang, J. L. Zeng, X. Wang and T. Y. Zhu, *Rsc Adv.*, 2015, **5**, 52066-52071.
17. A. Rokicinska, P. Natkanski, B. Dudek, M. Drozdek, L. Litynska-Dobrzynska

and P. Kustrowski, *Appl. Catal. B-Environ.*, 2016, **195**, 59-68.

18. S. Zhao, K. Z. Li, S. Jiang and J. H. Li, *Appl. Catal. B-Environ.*, 2016, **181**, 236-248.

19. F. Y. Hu, Y. Peng, J. J. Chen, S. Liu, H. Song and J. H. Li, *Appl. Catal. B-Environ.*, 2019, **240**, 329-336.

20. Q. M. Ren, S. P. Mo, R. S. Peng, Z. T. Feng, M. Y. Zhang, L. M. Chen, M. L. Fu, J. L. Wu and D. Q. Ye, *J. Mater. Chem. A*, 2018, **6**, 498-509.

21. Q. M. Ren, Z. T. Feng, S. P. Mo, C. L. Huang, S. J. Li, W. X. Zhang, L. M. Chen, M. L. Fu, J. L. Wu and D. Q. Ye, *Catal. Today*, 2019, **332**, 160-167.

22. K. M. Ji, H. X. Dai, J. G. Deng, X. W. Li, Y. Wang, B. Z. Gao, G. M. Bai and C. T. Au, *Appl. Catal. A-Gen.*, 2012, **447**, 41-48.

23. J. G. Deng, L. Zhang, H. X. Dai and C. T. Au, *Appl. Catal. A-Gen.*, 2009, **352**, 43-49.

24. X. W. Li, H. X. Dai, J. G. Deng, Y. X. Liu, Z. X. Zhao, Y. Wang, H. G. Yang and C. T. Au, *Appl. Catal. A-Gen.*, 2013, **458**, 11-20.

25. J. G. Deng, H. X. Dai, H. Y. Jiang, L. Zhang, G. Z. Wang, H. He and C. T. Au, *Environ. Sci. Technol.*, 2010, **44**, 2618-2623.

26. S. A. C. Carabineiro, X. Chen, M. Konsolakis, A. C. Psarras, P. B. Tavares, J. J. M. Orfao, M. F. R. Pereira and J. L. Figueiredo, *Catal. Today*, 2015, **244**, 161-171.

27. Q. Yang, W. Dong, C. Wang, X. Li, K. Li, P. Yue and J. Li, *Catal. Sci. Technol.*, 2018, **8**.

28. Y. X. Liu, H. X. Dai, J. G. Deng, L. Zhang, Z. X. Zhao, X. W. Li, Y. Wang, S. H. Xie, H. G. Yang and G. S. Guo, *Inorg. Chem.*, 2013, **52**, 8665-8676.

29. X. W. Li, H. X. Dai, J. G. Deng, Y. X. Liu, S. H. Xie, Z. X. Zhao, Y. Wang, G. S. Guo and H. Arandiyan, *Chem. Eng. J.*, 2013, **228**, 965-975.

30. H. L. Chen, G. L. Wei, X. L. Liang, P. Liu, H. P. He, Y. F. Xi and J. X. Zhu, *Appl. Surf. Sci.*, 2019, **489**, 905-912.

31. K. Niu, L. M. Liang, J. S. Li and F. Zhang, *Micropor. Mesopor. Mat.*, 2016, **220**, 220-224.

32. D. Y. Yoon, E. Lim, Y. J. Kim, J. H. Kim, T. Ryu, S. Lee, B. K. Cho, I. S. Nam, J. W. Choung and S. Yoo, *J. Catal.*, 2014, **319**, 182-193.

33. S. Palimar, S. D. Kaushik, V. Siruguri, D. Swain, A. E. Viegas, C. Narayana and N. G. Sundaram, *Dalton T.*, 2016, **45**, 13547-13555.

34. F. Kleitz, F. Berube, R. Guillet-Nicolas, C. M. Yang and M. Thommes, *J. Phys. Chem. C*, 2010, **114**, 9344-9355.

35. Z. Zhu, Y. Shi, C. Aruta and N. Yang, *ACS Applied Energy Materials*, 2018, **1**, 5308-5317.

36. N. A. Merino, B. P. Barbero, P. Eloy and L. E. Cadus, *Appl. Surf. Sci.*, 2006, **253**, 1489-1493.

37. H. Chen, W. Cui, D. Li, Q. Tian, J. He, Q. Liu, X. Chen, M. Cui, X. Qiao, Z. Zhang, J. Tang and Z. Fei, *Ind. Eng. Chem. Res.*, 2020, **59**, 10804-10812.

38. R. L. Fomekong and B. Saruhan, *Front. Mater.*, 2019, **6**, 252.

39. Y. C. Zhang, Z. Li, L. Zhang, L. Pan, X. Zhang, L. Wang, A. F. and J. J. Zou, *Appl. Catal. B-Environ.*, 2017, **224**, 101-108.

40. N. Zhang, X. Li, H. Ye, S. Chen, H. Ju, D. Liu, Y. Lin, W. Ye, C. Wang and Q. Xu, *J. Am. Chem. Soc.*, 2016, **138**, 8928 − 8935.

41. T. Saitoh, T. Mizokawa, A. Fujimori, M. Abbate, Y. Takeda and M. Takano, *Phys. Rev. B,* 1997, **55**, 4257-4266.

42. A. Grimaud, O. Diaz-Morales, B. Han, W. T. Hong, Y. L. Lee, L. Giordano, K. A. Stoerzinger, M. T. M. Koper and Y. Shao-Horn, *Nat. Chem.*, 2017, **15**, 121-126.

43. A. Grimaud, A. Demortière, M. Saubanère, W. Dachraoui, M. Duchamp, M. L. Doublet and J. M. Tarascon, *Nat. Energ.*, 2017, **2**, 16189.

44. B. Hammer and J. K. Norskov, *Nature*, 1995, **376**, 238-240.

45. A. Grimaud, K. J. May, C. E. Carlton, Y. L. Lee, M. Risch, W. T. Hong, J. G.

Zhou and Y. Shao-Horn, *Nat. Commun.*, 2013, **4**, 2439.

46. J. F. Moulder, J. Chastain and R. C. King, *Chem. Phys. Lett.*, 1992, **220**, 7-10.

47. H. Liang, Y. X. Hong, C. Q. Zhu, S. H. Li, Y. Chen, Z. L. Liu and D. Q. Ye, *Catal. Today*, 2013, **201**, 98-102.

48. J. K. Nørskov, F. Studt, F. Abild-Pedersen and T. Bligaard, *Wiley Online Library*, 2014.

49. L. Wang, Z. Huang, Y. Du, S. Guo and G. Jing, *Chem. Commun.*, 2021, **57**, 4942-4945.